Title

Rapid Vapor-Driven Plasma Contamination and Suppressed Net Lithium Surface Loss in the HIDRA Stellarator

Journal

Journal of Fusion Energy, 45(1)

ISSN

0164-0313

Authors

Rizkallah, Rabel

Shone, Andrew

O'Dea, Daniel

et al.

Publication Date

2026-06-10

DOI

10.1007/s10894-026-00582-y

Journal of Fusion Energy (2026) 45:39
https://doi.org/10.1007/s10894-026-00582-y

RESEARCH

Rapid Vapor-Driven Plasma Contamination and Suppressed Net Lithium Surface Loss in the HIDRA Stellarator

Rabel Rizkallah[1,2] · Andrew Shone[1,3] · Daniel O'Dea[1,3] · Davide Curreli[1] · Daniel Andruczyk[1]

Received: 10 December 2025 / Accepted: 25 May 2026

Abstract

Experiments in the HIDRA stellarator show that the inferred lithium net-loss suppression factor R_{eff}, which absorbs effects from redeposition, recycling, and slow evaporation, remains between 0.91 and unity across hydrogen and helium plasmas. This implies a lithium lifetime far longer than would be expected from the evaporation rate alone. Lithium surface temperature locking appears only intermittently, and high-temperature operation consistently drives lithium release that overwhelms the available fueling. As a result, the plasma transitions quickly to a lithium-dominated regime, preventing sustained operation in vapor-shielding-relevant conditions. Despite HIDRA's relatively low densities and particle fluxes, these findings highlight that unmitigated lithium vapor readily contaminates the confined plasma, underscoring the need for active capture or control to achieve stable lithium-based plasma–material interaction regimes.

Keywords Lithium · Liquid metal PFCs · Temperature locking · Plasma contamination

Introduction

Power exhaust remains one of the most critical challenges for magnetic confinement fusion reactors [1] with heat fluxes expected in reactor-grade divertors to exceed the thermal limits of conventional solid plasma-facing components (PFCs). Liquid metal (LM) concepts have therefore emerged as a potential solution, offering self-healing surfaces, tolerance to transient loads, and improved plasma-surface compatibility [2, 3]. Among these, lithium (Li) has attracted particular interest due to its low melting temperature, low atomic number, and beneficial effects on plasma performance.

Lithium coatings and liquid lithium limiters have demonstrated marked improvements in confinement and plasma purity across multiple tokamak devices. Early work on the Tokamak Fusion Test Reactor (TFTR) and National Spherical Torus Experiment (NSTX) showed that lithium acts as a strong getter, effectively reducing wall recycling and lowering edge neutral density [4, 5]. Subsequent experiments on the Frascati Tokamak Upgrade (FTU) reported increased core density and up to 20% longer confinement times with lithium limiters [6], while results from the Lithium Tokamak Experiment (LTX) showed flatter edge temperature profiles under lithiated conditions [7]. These effects are typically attributed to reduced hydrogen (H) recycling and impurity content, which together lead to lower edge temperature gradients and improved global confinement [8, 9]. Lithium has also been linked to ELM mitigation and pacing, where small lithium injections at the plasma edge suppress large type-I ELMs by triggering smaller, more frequent bursts [10, 11].

However, despite these advantages, lithium's high vapor pressure and chemical reactivity constrain its operational temperature window. Modeling and experiments suggest that temperatures between $670 - 720\,\mathrm{K}$ mark the transition between low- and high-recycling regimes [12], while excessive evaporation above $970\,\mathrm{K}$ can contaminate the plasma [13]. Safety considerations further exclude water cooling, and the strong lithium-hydrogen affinity that aids recycling control also introduces tritium (T) retention concerns. In reactor-scale systems such as ITER or DEMO,

✉ Rabel Rizkallah
rrizkallah@ucsd.edu

[1] Center for Plasma-Material Interactions, Department of Nuclear, Plasma and Radiological Engineering, University of Illinois Urbana-Champaign, Urbana, IL 61801, USA

[2] Present address: University of California San Diego (UCSD), La Jolla, San Diego, CA 92093, USA

[3] Present address: Tokamak Energy Inc., Washington, DC 20024, USA

Published online: 10 June 2026

this necessitates active tritium recovery, for which several approaches have been proposed, including thermal desorption and centrifugal separation of Li-T compounds [14, 15]. Nonetheless, reliable control of lithium inventory and retention remains an open technological challenge.

Another promising feature of lithium-based PFCs is the phenomenon of *vapor shielding*. Under intense plasma bombardment, lithium evaporation can form a vapor cloud between the plasma and the target surface. This vapor layer radiates and dissipates a substantial fraction of the incident energy, reducing the net heat load on the PFC and effectively increasing its power-handling capability [16, 17]. Early theoretical work by Sestero on high-Z vapor blankets anticipated this radiative buffering effect [18], later confirmed in experiments with liquid tin [19] and lithium [20]. Measurements have shown that the surface temperature of liquid tin [19] or lithium [21, 22] "locks" around $1070 - 1170\,\mathrm{K}$, remaining nearly constant even as the upstream plasma flux increases. This arises from the dynamic balance between plasma heating, evaporation, and cooling through excitation, ionization, and recombination in the vapor cloud [23]. Vapor shielding can also drastically decrease the net evaporation from the liquid metal surface and thereby increase the temperature operational window [2], which is very important for lithium. Both modeling and experiments have demonstrated that vapor shielding can dramatically reduce net lithium evaporation when the lithium redeposition fraction approaches unity. Using the redeposition-aware power-balance model of [24] together with lithium-supply constraints from [25] suggests tolerable incident heat fluxes of order ~ 20 MW m^{-2} for Magnum-PSI conditions, and potentially exceeding 100 MW m^{-2} in tokamak-relevant regimes where the dissipated energy per lithium particle is higher, albeit at evaporative fluxes that may be challenging for reactor operation. In this work we quantify a *net-loss factor* f, defined as the ratio of the observed net lithium loss to that predicted by a reference evaporation source model, and define its complement $R_{\mathrm{eff}} = 1 - f$ which parameterizes the reduction of net lithium loss from the surface relative to the reference evaporation model. By construction, R_{eff} absorbs both local recycling/return of lithium and any reduction of the effective evaporation rate due to surface conditioning. This makes R_{eff}, and equivalently f, a key metric for lithium PFC viability.

Recent experiments on Magnum-PSI have validated several key elements of lithium vapor-shielding phenomenology, including locked surface temperatures and tolerance of transient ELM-like loads up to 0.75 MJ m^{-2} [20, 21]. However, these studies also revealed discrepancies between modeled and measured surface temperatures unless redeposition effects and radiation from returning lithium particles were included. Furthermore, surface analyses indicate that a LiD layer can persist up to $1120\,\mathrm{K}$ [21], well above the expected deuterium desorption temperature [26, 27], suggesting complex surface chemistry that could affect both flow and evaporation.

Despite substantial progress, the physics of lithium vapor shielding and redeposition remains incompletely understood. In particular, the spatial distribution of the vapor, its influence on plasma parameters, and the dynamics of lithium reattachment to the surface are still uncertain. These processes are central to determining whether lithium can provide reliable and safe operation in reactor-relevant regimes. The present work probes net lithium surface loss and lithium-driven cooling signatures in the HIDRA classical stellarator, where controlled experiments on lithium-coated surfaces are conducted under steady-state hydrogen and helium plasma conditions. We infer f and R_{eff} from a mass-balance approach and interpret these metrics in the context of local recycling/return, surface conditioning, and plasma contamination constraints.

Methods

The Hybrid Illinois Device for Research and Applications (HIDRA) is a mid-sized classical $l = 2$ stellarator with a five-fold toroidal symmetry [28]. The device has a major radius $R_0 = 72\ \mathrm{cm}$ and minor radius $a = 19\ \mathrm{cm}$, and is equipped with microwave heating up to 21 kW. HIDRA operates at magnetic fields up to ~ 1 T and has demonstrated continuous steady-state operation for up to 180 minutes in the low-field regime ($\lesssim 0.1$ T).

The conducted experiments aimed at assessing lithium operational regimes and net lithium loss from the surface in a toroidal magnetic geometry. Lithium samples were introduced using the HIDRA Material Analysis Test-stand (HIDRA-MAT), an in-situ exposure system attached to HIDRA [29]. Figure 1 shows a top view schematic of the HIDRA vessel, with the location of HIDRA-MAT and supporting diagnostics: spectrometers, RGAs, pressure gauges, and reciprocating Langmuir probe. The two turbo pumps of HIDRA are located approximately on the south- and north-facing sides of the stellarator and referred to as the "south turbo" and "north turbo", respectively. Lithium droplets were deposited on a tungsten disk (15 mm diameter, 3 mm thick) inside HIDRA-MAT and allowed to wet the surface (see Fig. 2), before transferring the sample into the main chamber for plasma exposure. A thermocouple positioned $\sim 1 - 2$ mm below the surface monitored the sample temperature. Diagnostics included an Ocean Insight HR2000 spectrometer, SRS100 residual gas analyzers, Pfeiffer PKR 251 pressure gauges, cameras, and a reciprocating Langmuir probe for edge T_e and n_e profiles.

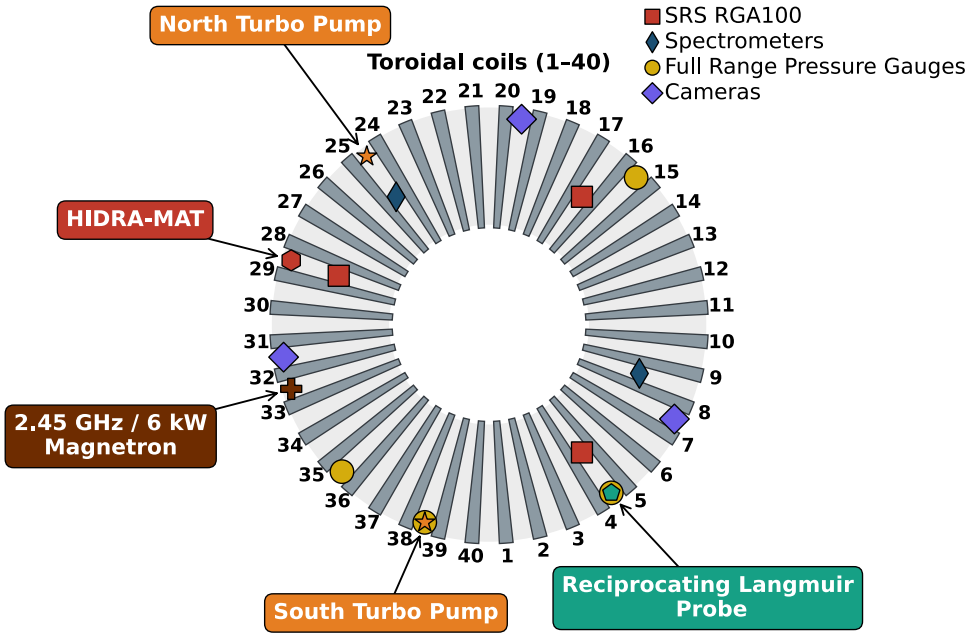

Fig. 1 Top view schematic of the HIDRA vessel and main diagnostics location

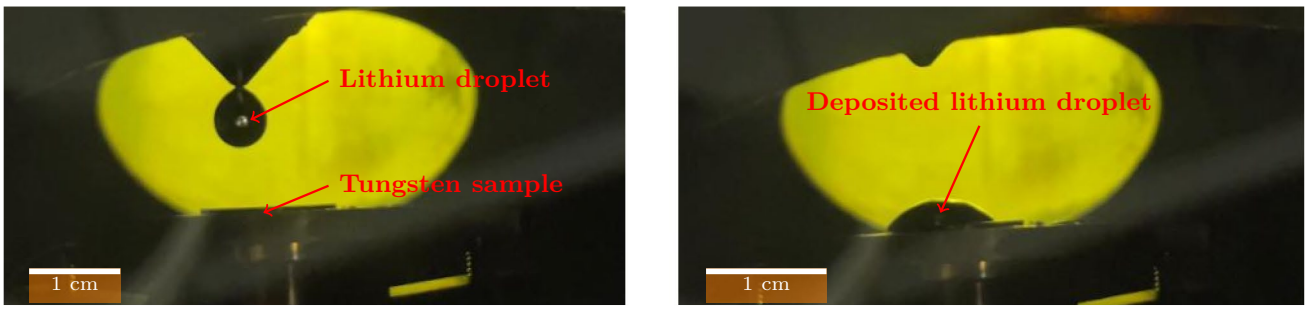

Fig. 2 Left: application of a lithium droplet onto the tungsten target in HIDRA-MAT. Right: lithium wetting of the tungsten sample

HIDRA plasmas were stable and reproducible under fixed operating conditions and initial reference plasmas were obtained before lithium introduction. The rotational transform was held near $\iota/2\pi \approx 1/3$ for consistency with prior PMI campaigns. The experimental sequence included a power scan at 20%, 50%, and 90% forward power on the 6 kW magnetron and variation of the radial sample position. In practice, lithium injection disrupted plasma stability at magnetron powers above 20%, limiting high-power shots. Sample position adjustments were guided by thermocouple trends to control lithium evaporation.

Plasma Characteristics

The HIDRA magnetic topology has been previously mapped and reproduced computationally [30]. Using the methodology described in [31], the Edge Monte-Carlo 3D (EMC3) code [32, 33] was used to estimate heat and particle fluxes to a sample mounted on HIDRA-MAT. Simulations employed a magnetic grid including the measured error field and assumed 6 kW microwave heating, since only the low-power magnetron was operational during this campaign. The modeled fluxes indicate that the side surface of a sample in the near scrape-off layer receives the highest incident heat due to local field-line orientation. With 6 kW of input power, front-surface heat fluxes where the lithium is deposited peak near 30 kW/m^2, while side-surface fluxes reach ∼400 kW/m^2. Particle fluxes are correspondingly low, on the order of $10^{22}\,\mathrm{m}^{-2}\,\mathrm{s}^{-1}$ on the front surface and $10^{23}\,\mathrm{m}^{-2}\,\mathrm{s}^{-1}$ on the side. We note that the modeled heat fluxes are orders of magnitude lower than those in linear plasma devices or tokamak divertors where vapor shielding is typically discussed. Nevertheless, the observed plateau temperatures are comparable to the locking temperatures reported in lithium vapor-shielding experiments in these higher-flux devices. In this work we therefore use the term “temperature locking” to describe a plateau consistent with strong lithium-driven evaporative and radiative cooling, without claiming a fully developed vapor-shielding regime.

Electron temperature and density were measured using a reciprocating Langmuir probe with a tungsten tip of 5 mm

length and 0.96 mm diameter. The ion current in HIDRA does not exhibit clear saturation, consistent with observations from WEGA and attributed to the presence of a fast-electron population [34, 35]. A two-temperature Maxwellian electron distribution is therefore assumed. Following Stangeby's formulation [36], the probe current in such plasmas can be written as:

$$I = I^i_{sat}\Bigg\{1 - \frac{\sqrt{2m_i/\pi m_e}}{1+f_n}\times \Bigg[(1-\sigma_s)\exp\left(\frac{e\,(V-V_p)}{k_B T_{es}}\right) + (1-\sigma_f)\,f_n\sqrt{f_T}\exp\left(\frac{e\,(V-V_p)}{k_B T_{es} f_T}\right)\Bigg]\Bigg\}, \tag{1}$$

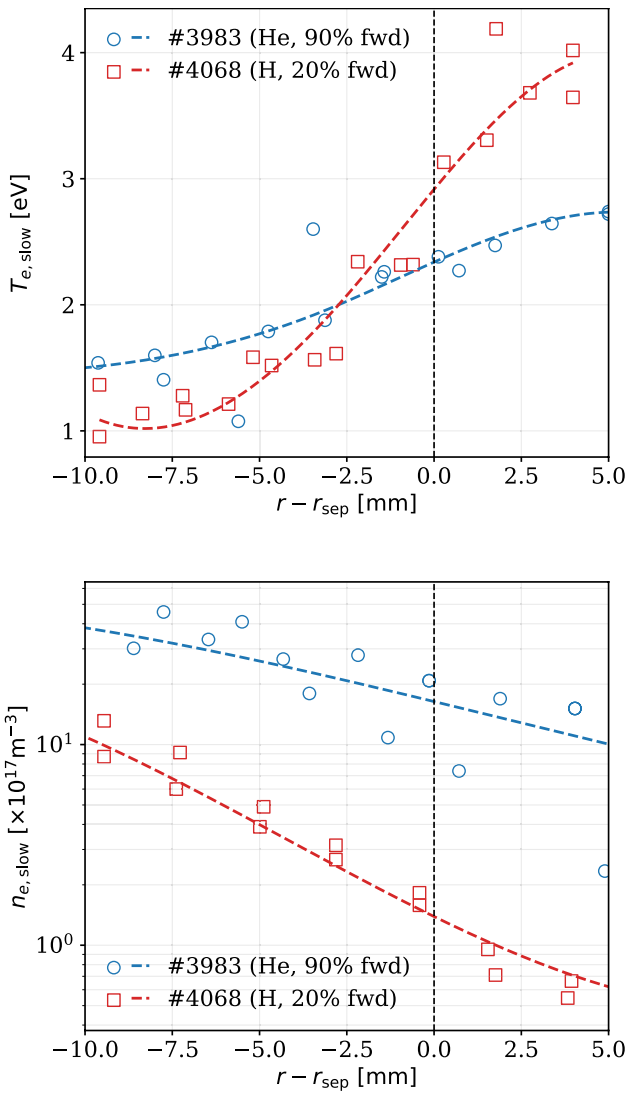

Fig. 3 Slow electrons T_e (top) and n_e (bottom) profiles in a hydrogen plasma at 20% forward power (shot #4068) and a helium plasma at 90% forward power (shot #3983), versus the distance from the separatrix $r - r_{sep}$. The vertical dashed line indicates the separatrix location

where I^i_{sat} is the ion saturation current, f_n is the density ratio of the fast electrons to the slow electrons, f_T is the temperature ratio of the two electron components, V is the probe bias voltage, σ_s and σ_f are respectively the secondary electron emission coefficient for the slow and fast electrons, and T_{es} is the temperature of the slow electrons. Neglecting secondary-electron emission, Eq. (1) provides robust fits to HIDRA probe traces. Typical results show slow-electron temperatures of $1-5$ eV and fast-electron temperatures near 180 eV, with $f_n < 0.05$. Example profiles for hydrogen and helium plasmas are shown in Fig. 3. The electron temperature increases near the last closed flux surface (LCFS), particularly in hydrogen plasmas, and then decreases toward the magnetic axis, a behavior consistent with past WEGA findings [34, 35]. Electron densities typically range from 10^{18} to 5×10^{18} m^{-3} inside the LCFS, and between 10^{17} and 10^{18} m^{-3} in the near scrape-off layer, which is more relevant for the HIDRA-MAT exposures.

Results

Net Lithium Evaporation and Loss-Reduction Fraction R_{eff}

Net lithium loss factors were estimated for shots in which both the initial and final lithium masses could be quantified. We infer the net-loss factor f and report its complement $R_{\mathrm{eff}} = 1 - f$, which we interpret as an effective loss-reduction fraction which would absorb effects of prompt redeposition, recycling and slow evaporation due to surface contamination. The initial lithium inventory was determined from the droplet size and the lithium evaporation rate inferred from the surface temperature. Thermocouples mounted $1-2$ mm below the tungsten surface recorded sub-surface temperatures; these were taken as representative of the lithium surface temperature. The initial lithium mass was estimated from camera images by spatially calibrating each image using the known tungsten sample size, extracting the two-dimensional droplet profile, and revolving that profile about its symmetry axis to reconstruct the droplet volume. The lithium mass was then obtained by multiplying the reconstructed volume by the lithium density at the relevant temperature. The lithium mass per droplet obtained from this image-based method was validated against earlier calibration depositions for which the mass of a single droplet was measured directly, showing good agreement. We therefore report the initial lithium amounts with an estimated uncertainty of ∼15%.

The lithium evaporative flux $J^{\mathrm{vap}}_{\mathrm{Li}}(T)$ is used here as an effective mapping between the measured sample temperature and an estimated lithium particle source, consistent

with published lithium evaporation datasets and with evaporative formulations adopted in prior experimental [37] and numerical [38, 39] PMI studies. A practical motivation for using a fitted expression rather than a direct vapor-pressure model is to remain consistent with these established datasets and models. In this work we use the following temperature-dependent relation for $J_{\mathrm{Li}}^{\mathrm{vap}}$:

$$\log_{10}[J_{\mathrm{Li}}^{\mathrm{vap}}(T)] = a - \frac{b}{T} + \frac{d}{1+\exp\left(-\frac{T-c}{s}\right)}. \tag{2}$$

where $J_{\mathrm{Li}}^{\mathrm{vap}}$ is in $\mathrm{m^{-2}\,s^{-1}}$, T is the lithium surface temperature in K, and a, b, c, d, and s are fitting coefficients listed in Table 1. The reported coefficients are rounded for readability; the fit function itself is what is used in the subsequent analysis. Over the temperature window accessed in this campaign, this fit remains in good agreement with fluxes implied by standard lithium vapor-pressure correlations via Hertz–Knudsen/Langmuir estimates.

With the defined net-loss factor f and R_{eff} fraction, the net evaporative loss is given by the relation:

$$\Gamma_{\mathrm{net}} = f\,\Gamma_{\mathrm{Li}} = (1 - R_{\mathrm{eff}})\,\Gamma_{\mathrm{Li}}, \tag{3}$$

where Γ_{Li} is the total lithium evaporation source from the droplet:

$$\Gamma_{\mathrm{Li}} = A_d\,J_{\mathrm{Li}}^{\mathrm{vap}}(T), \tag{4}$$

and A_d is the exposed lithium surface area estimated from the camera images of the deposited droplet. Both Γ_{net} and Γ_{Li} and particle fluxes in units of $\mathrm{s^{-1}}$. Curvature-dependent corrections to the evaporation rate are expected to be negligible for the mm-scale droplets used here and are not included. For simplicity we treat the exposed lithium area A_d as constant over the interval used to define t_{evap}. In reality, the droplet shape and exposed area may evolve during evaporation and surface conditioning such as oxide and hydride formation may modify the effective evaporation rate. These effects are not explicitly modeled here and are absorbed into the effective mass-balance estimate of f, and thus R_{eff}. The values of R_{eff} reported later on are therefore effective mass-balance estimates over t_{evap}.

The total number of lithium atoms initially present in a lithium droplet is:

Table 1 Fitting coefficients for Eq. (2). Values are rounded for readability

a	b [K]	d	c [K]	s [K]
30.6	7.12×10^3	1.0	690	100

$$N_{\mathrm{Li}} = V_d\,\frac{\rho_{\mathrm{Li}}(T)}{m_{\mathrm{Li,atom}}}, \tag{5}$$

where V_d is the droplet volume, $m_{\mathrm{Li,atom}}$ is the mass of one lithium atom, and ρ_{Li} is the lithium mass density obtained in $\mathrm{kg\,m^{-3}}$ from [40–42] as:

$$\rho_{\mathrm{Li}}(T) = -9.74 \times 10^{-2}\,T + 560.5, \tag{6}$$

with T the temperature in K.

By completely evaporating the lithium droplet over a measured time interval t_{evap}, identified from the inflection point in the surface-temperature trace, mass conservation gives:

$$N_{\mathrm{Li}} = \Gamma_{\mathrm{net}}\,t_{\mathrm{evap}} = f\,\Gamma_{\mathrm{Li}}\,t_{\mathrm{evap}}. \tag{7}$$

Rearranging, the net-loss factor is:

$$f \approx \frac{N_{\mathrm{Li}}}{\Gamma_{\mathrm{Li}}\,t_{\mathrm{evap}}} \approx \frac{N_{\mathrm{Li}}}{J_{\mathrm{Li}}^{\mathrm{vap}}(T)\,A_d\,t_{\mathrm{evap}}}, \tag{8}$$

and therefore R_{eff} is given by:

$$R_{\mathrm{eff}} \approx 1 - \frac{N_{\mathrm{Li}}}{J_{\mathrm{Li}}^{\mathrm{vap}}(T)\,A_d\,t_{\mathrm{evap}}}. \tag{9}$$

Figure 4 shows the temperature evolution for a helium discharge at 90% forward power with the sample positioned 18 mm from the LCFS. Shot #4184 is the reference shot (no lithium on the sample) and shot #4194 is the shot with the lithium sample. The inflection point in the temperature trace marks the time at which the droplet has fully evaporated. Shot #4194 was preceded by two shots involving the same lithium droplet; although the earlier shots were farther from the LCFS and produced limited evaporation, the combined mass balance over all three shots yields a loss-reduction fraction of approximately $R_{\mathrm{eff}} = 0.91$. Effective R_{eff} fractions for subsequent lithium shots were determined in the same manner by combining temperature profiles with RGA and spectroscopic signatures of lithium release. The results are summarized in Table 2.

Of the inferred R_{eff} fractions, one case (shot #4330) has R_{eff} tending toward unity within the mass-balance uncertainty (equivalently $f \to 0$), while the remaining values all show high $R_{\mathrm{eff}} \geq 0.91$ ($f \leq 0.09$). The exceptional value for shot #4330 corresponds to the smallest gap between the lithium sample and the plasma (12 mm from the LCFS within uncertainty). At this proximity, the sample may have acted as a limiter with enhanced plasma–surface interaction. Evaporated Li can then ionize close to the sample and be guided by magnetic/sheath fields to re-impact nearby

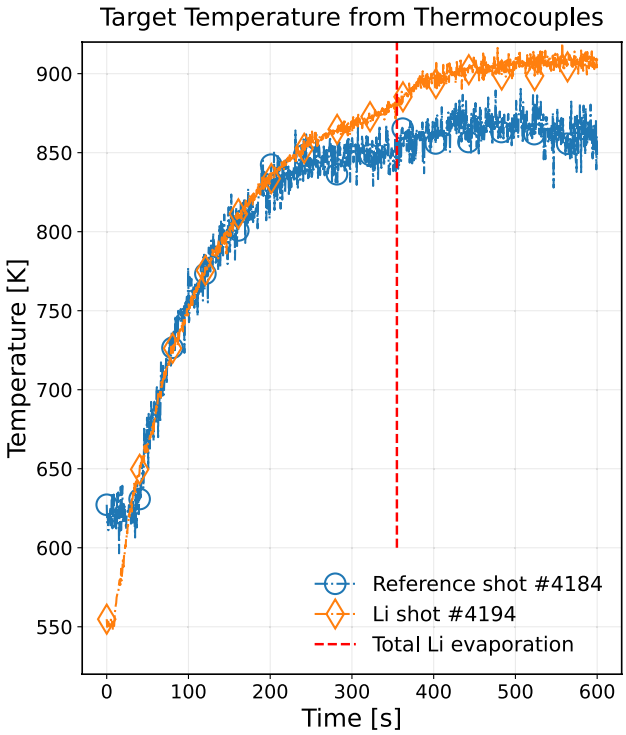

Fig. 4 Sample temperature profiles from thermocouples for the reference (#4184) and lithium (#4194) shots. The red vertical dashed line indicates the point where all the lithium has been evaporated

surfaces (including the sample), increasing the inferred R_{eff} from the mass balance. The other values greater than 0.9 are numerically similar to redeposition fractions reported in [43], but given the very different plasma conditions this comparison should be regarded as qualitative only. We however emphasize that R_{eff} inferred from Eq. (9) is an effective, model-referenced metric: while $R_{\text{eff}} \approx 1$ can reflect true local recycling/return of lithium in the HIDRA-MAT/sample environment, including redeposition, it can also reflect suppressed effective evaporation relative to the reference $J_{\text{Li}}^{\text{vap}}(T)$ due to surface conditioning with possible oxide or hydride layers formation.

Using edge conditions $T_e \sim 2$–3 eV and $n_e \sim 10^{17}$–10^{18} m^{-3}, and a lithium surface temperature $T \sim 800$–1000 K (neutral thermal speed $v_{\text{Li}} \sim 1$–2 km s^{-1}), the characteristic distance before an electron-impact process k (excitation or ionization) is $\lambda_k \simeq v_{\text{Li}}/(n_e\langle\sigma v\rangle_k)$, where the rate coefficient $\langle\sigma v\rangle_k$ is taken from standard lithium electron-impact atomic data. For the above n_e range, Li-I excitation lengths are typically $\lambda_{\text{exc}} \sim$ mm–cm, consistent with Li-I emission arising close to the sample. Ionization is more sensitive to the electron-energy distribution: a purely Maxwellian edge with $T_e \sim 2$–3 eV can imply much longer λ_{ion}, whereas the existing fast electron population reduces λ_{ion} to the cm–10^2 cm range. Heavy-particle scattering can be estimated from kinetic theory as $\lambda_{nn} \simeq (n_n\sigma_{nn})^{-1}$ with ~ 4–40 cm characteristic distances. Overall, these mm–cm scales are comparable to the HIDRA-MAT and sample dimensions, supporting near-sample excitation and possibly ionization as well as local return/recycling pathways contributing to suppressed net lithium loss as captured by R_{eff}.

Temperature Locking

Several HIDRA shots exhibit temperature locking consistent with strong lithium-driven cooling, including evaporative losses and enhanced radiative/ionization losses evidenced by the growth of Li-I/Li-II emission and visible lithium plasma. Similar temperature-limiting behavior has been reported in vapor-shielding studies on other devices, albeit typically at much higher plasma heat fluxes than in HIDRA. Because a temperature plateau can arise under steady heat flux without a directly observed near-surface vapor cloud formation, we interpret the present observations conservatively as lithium-driven cooling rather than definitive evidence of a vapor-shielding regime.

Shot #4068 shows clear evidence of temperature locking. Conducted at 20% forward power in a hydrogen plasma, the sample was advanced toward the plasma in 1 mm steps, from a 3 cm to a 1.8 cm distance from the separatrix (attained 2250 seconds into the shot), where a steep temperature rise occurred, holding the position thereafter. This resulted in a locked surface temperature around 1030 K.

In a similar hydrogen plasma shot also with 20% forward power (shot #4330), the sample was progressively advanced from 3 cm distance from the separatrix to 1.4 cm at the 720 seconds mark and kept there for the remainder of the shot. The lithium surface rose to nearly 970 K before abruptly rising to $\sim$ 1030 K before the shot terminated. It is unclear whether this jump reflects depletion of the lithium layer, a sudden increase in plasma flux, or a bad thermal contact at the thermocouple junction. The rapidity of the increase compared to other shots suggests the latter is more likely, with the 1030 K matching the temperature lock achieved

Table 2 Effective R_{eff} fractions estimates

Shot number	Plasma gas	Initial lithium amount (mg)	R_{eff} fractions
4192–4194	He	63 ± 9	0.91
4303–4304	H	85 ± 13	0.96
4311	H	84 ± 13	0.92
4330	H	63 ± 9	≥ 0.999(point estimate: $R_{\text{eff}}^{\text{calc}} = 0.999944$)

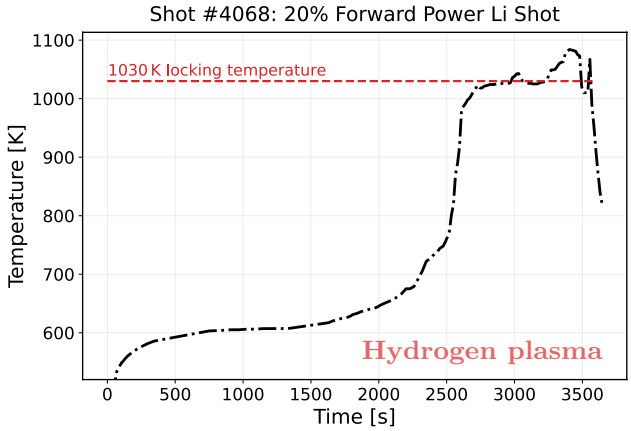

Fig. 5 Surface temperature time evolution during shot #4068 under a hydrogen plasma

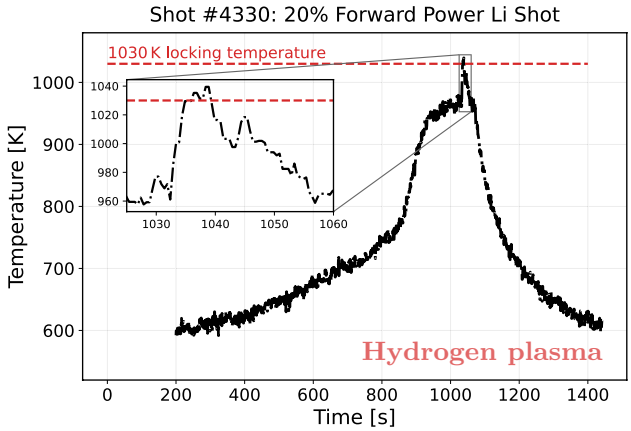

Fig. 6 Surface temperature time evolution during shot #4330 under a hydrogen plasma

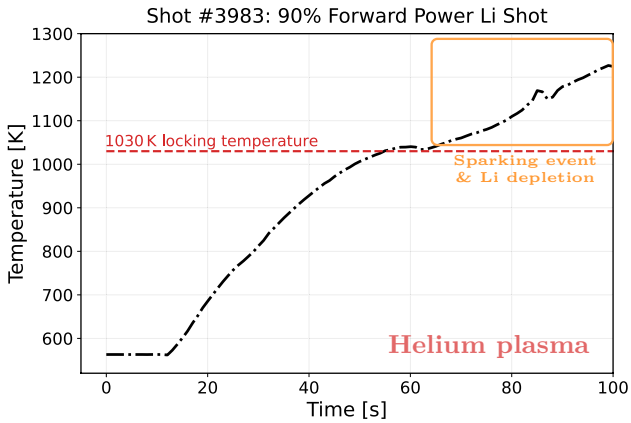

Fig. 7 Surface temperature time evolution during shot #3983 under a helium plasma

in shot #4068. The corresponding time traces are shown in Figs. 5 and 6.

The locking temperature was also observed in a helium discharge (shot #3983) at 90% forward power. During this discharge however, the plasma entered a period of unstable behavior accompanied by widespread visible sparking inside the HIDRA vessel. This event led to the rapid depletion of the lithium layer, after which the sample temperature rose above the 1030 K locking temperature. The corresponding surface temperature evolution is shown in Fig. 7.

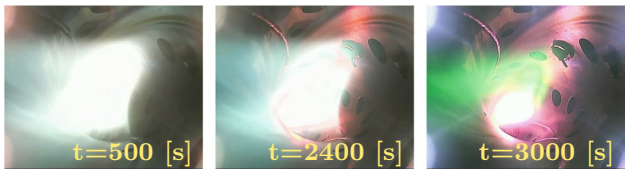

Fig. 8 Progressive lithium contamination (from left to right) during shot #4068

Lithium Contamination

Pushing for vapor shielding studies on HIDRA reveals challenges arising from the high lithium evaporation rates. Because the device typically operates with gas flow rates of only a few standard cubic centimeters per minute, lithium evaporation can rapidly become the dominant particle source. Figure 8 illustrates the transition observed in shot #4068 from a hydrogen plasma to one dominated by lithium emission as evaporation increased. The green emission in the final frame of Fig. 8 corresponds to the Li-II 548 nm line, indicating the presence of a lithium ion population. The appearance of Li-II is consistent with the hot-electron tail characteristic of HIDRA plasmas. Its emergence and the strong growth of Li-I/Li-II line emission imply that lithium excitation and ionization channels are active, providing radiative and ionization power sinks in addition to latent-heat removal by evaporation. As lithium became dominant, the hydrogen line intensities diminished, as shown in the spectrometer data of Fig. 9. All three detected hydrogen visible lines from the Balmer series (Hα, Hβ and Hγ) dropped during the high lithium evaporation phase, combined with a strong increase in the 610 nm and 670 nm lithium neutral lines and in the Li-II 548 nm line. The lithium ion signal persisted until shortly before the lithium on the sample was exhausted. During this phase, the chamber pressure decreased by nearly an order of magnitude (Fig. 10), with no loss of microwave power or increase in reflected power observed.

Lithium contamination also occurred during helium discharges, though to a lesser extent. Shot #4194 (90% forward power), previously discussed, shows an even stronger Li-II signal than shot #4068 (Fig. 11), consistent with the higher plasma power. However, the neutral helium line intensities did not decrease as dramatically as the hydrogen lines did in shot #4068. This difference can be explained from the high chemical reactivity of lithium with hydrogen, and from the

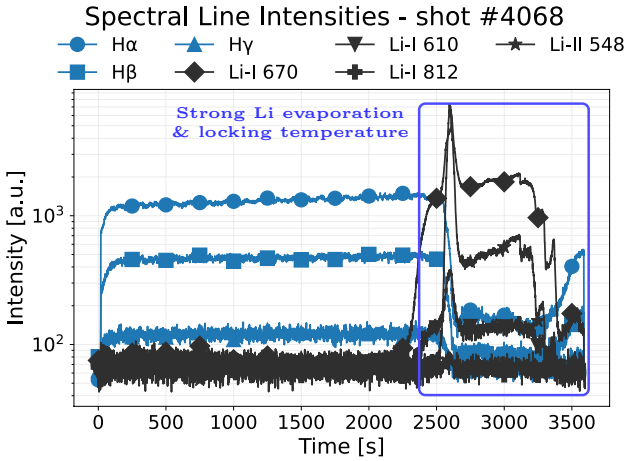

Fig. 9 Rise of the lithium emission intensities at the expense of the hydrogen emissions indicated in the blue rectangle, in correlation with the temperature time evolution of Fig. 6 for shot #4068

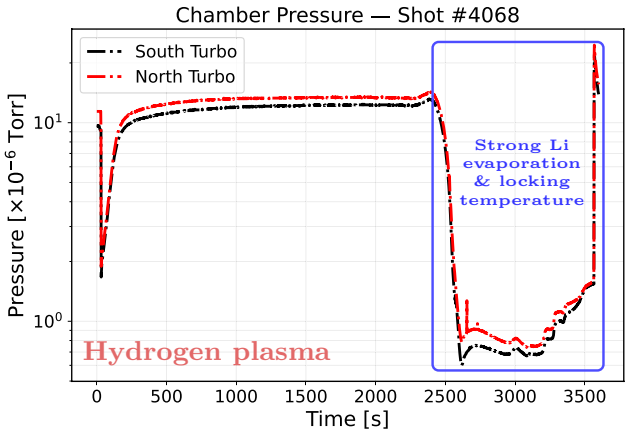

Fig. 10 Drop in the HIDRA chamber pressure measured at both south and north turbo pumps for shot #4068, indicated in the blue rectangle, coinciding with the strongest lithium evaporation rate at the 760°C surface locking temperature shown in Fig. 6

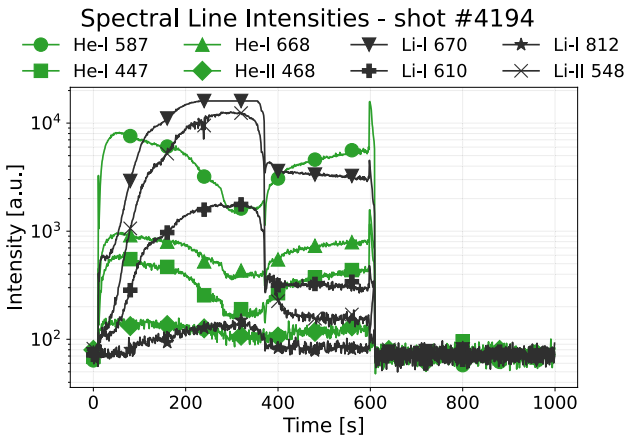

Fig. 11 Rise of lithium emission intensities and decrease of the helium emissions during shot #4194, in correlation with the temperature profile and RGA trends shown in Figs. 4 and 12 respectively

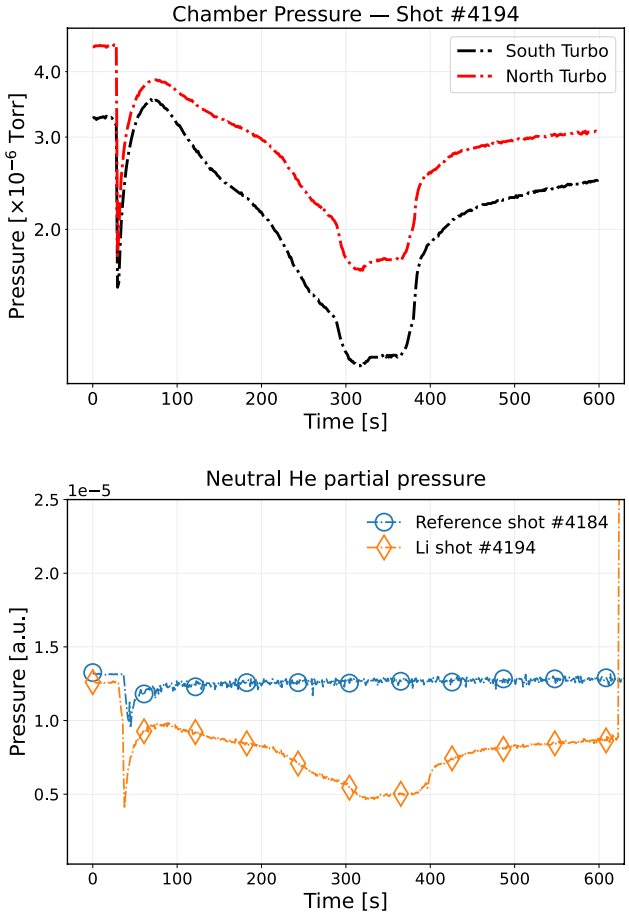

Fig. 12 Top: drop in the HIDRA chamber pressure for shot #4194 measured at both the south and north turbo pumps of HIDRA. Bottom: drop in the helium partial pressure as observed from the RGA traces during shot #4194 as compared to the reference shot #4184

lower lithium evaporation rate in shot #4194, which temperature remained approximately 100 K below that reached in shot #4068 (Fig. 4). Still, lithium rapidly became the dominant impurity in the plasma, with strong increases in the neutral 610 nm and 670 nm lithium lines and a small increase in the 812 nm line.

Lithium shots in helium generally exhibit characteristic pressure behavior. For shot #4194, in addition to the overall drop in chamber pressure attributed to lithium reacting with impurities, the helium partial pressure shows a marked decrease coincident with lithium entering the plasma. These profiles are shown in Fig. 12 with the pressure drop persisting until the lithium reservoir is depleted. Differences between the north and south pressure measurements resulted from a partially closed gate valve throttling the north turbo pump. A similar decrease in helium partial pressure during lithium exposure has been reported previously [44], where lithium-helium pumping was proposed as a possible mechanism. Further analysis of this phenomenon is presented

and discussed in [45], with new dedicated experiments still ongoing.

To assess whether HIDRA could tolerate low lithium evaporation rates without strong plasma contamination, additional experiments were performed with the lithium surface temperature restricted to $670 - 800\,\mathrm{K}$, well below the plateau temperatures observed in this study and below the conditions typically associated with vapor-shielding studies in higher-heat-flux devices. Figures 13 and 14 show results from hydrogen shots #4317 and #4322, both at 50% forward power. The temperature profiles are obtained from two thermocouples (TC1 and TC2), deployed on the downstream and upstream facing sides of the sample. Despite the low temperatures, both shots exhibited significant reductions in hydrogen line intensities concurrent with rising Li-I and Li-II signals. In Fig. 14, in particular, the decrease in the hydrogen lines correlates closely with the increase in the Li-II emission. Even at these modest temperatures, both the evaporation and thermal sputtering rates are several orders of magnitude larger than the hydrogen gas feed rate, resulting in rapid plasma dilution. Larger devices with higher fueling rates and higher plasma densities would be much less sensitive to such low levels of lithium evaporation. Experiments on Magnum-PSI, for example, operate with gas flows of order standard liters per minute, and no transition to a lithium plasma nor any Li-II emission was observed under similar lithium exposure conditions [22]. Although HIDRA can reach slightly higher electron temperatures (particularly near the LCFS) and supports a hot-electron population, the transition to a lithium-dominated plasma is primarily driven by the imbalance between lithium evaporation and the available fueling.

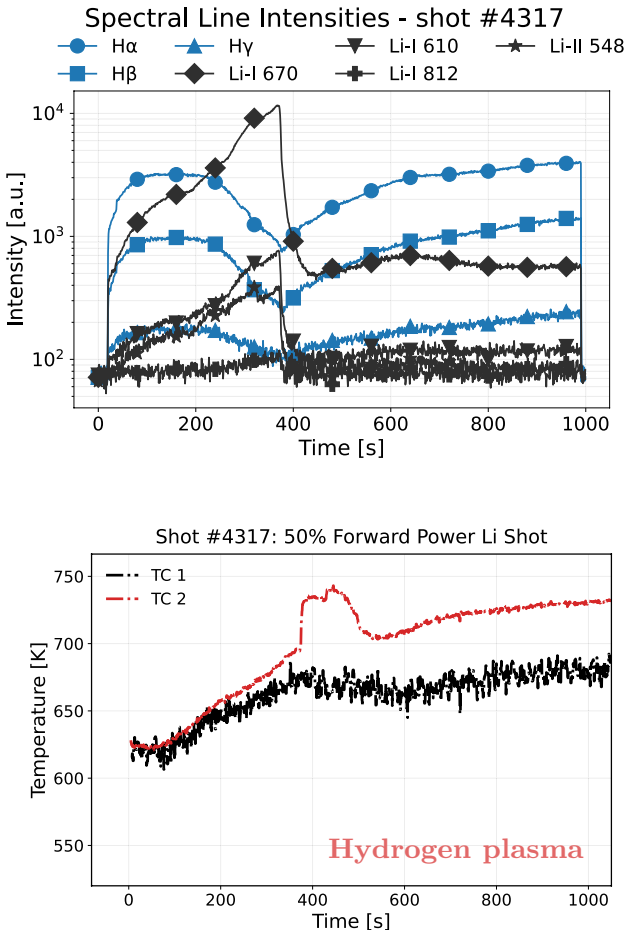

Fig. 13 Top: rise of lithium transitions at the expense of the hydrogen transitions during shot #4317. Bottom: corresponding surface temperature time evolution from both thermocouples (TC 1 and TC 2)

Mitigation strategies involve capturing lithium vapor before it reaches the plasma. Concepts such as the lithium vapor box [46, 47] employ geometric confinement and staged condensation to recycle lithium locally while preventing contamination of both the bulk plasma and device walls. Implementing a similar vapor-capture solution tailored to HIDRA would significantly broaden the accessible parameter space for future lithium experiments.

The observed transition from a hydrogen/helium plasma to a lithium-dominated plasma may involve additional physics beyond a simple neutral-flux ratio argument. Species-dependent confinement, changes to the local power balance induced by increased radiation from lithium, and altered ionization/recombination balance can modify temperatures and densities and thereby the observed emissions. Our data show strong correlation between evaporative timing, pressure/RGA drops, and lithium line growth, consistent with the evaporative-flux-dominated explanation, but the alternative mechanisms cannot be fully excluded without additional measurements.

Conclusions

Lithium experiments on the HIDRA classical stellarator yielded R_{eff} fractions ≥ 0.91 and net-loss factors $f \leq 0.09$, with one discharge exhibiting R_{eff} very close to unity. Because R_{eff} is inferred from a model-referenced mass balance, it should be interpreted as a net loss-suppression metric that absorbs effects of local recycling/return of lithium as well as suppressed effective evaporation due to surface conditioning.

Attempts to access vapor-shielding-relevant conditions in HIDRA revealed several challenges. Temperature plateaus/locking were observed in multiple discharges, but the temperature traces alone do not establish a vapor-shielded regime; we interpret them conservatively as lithium-driven cooling through evaporation and radiative/ionization losses. Even when the lithium surface temperature remained relatively low ($720 - 800\,\mathrm{K}$), far below the observed plateau temperatures, the evaporated lithium rapidly contaminated

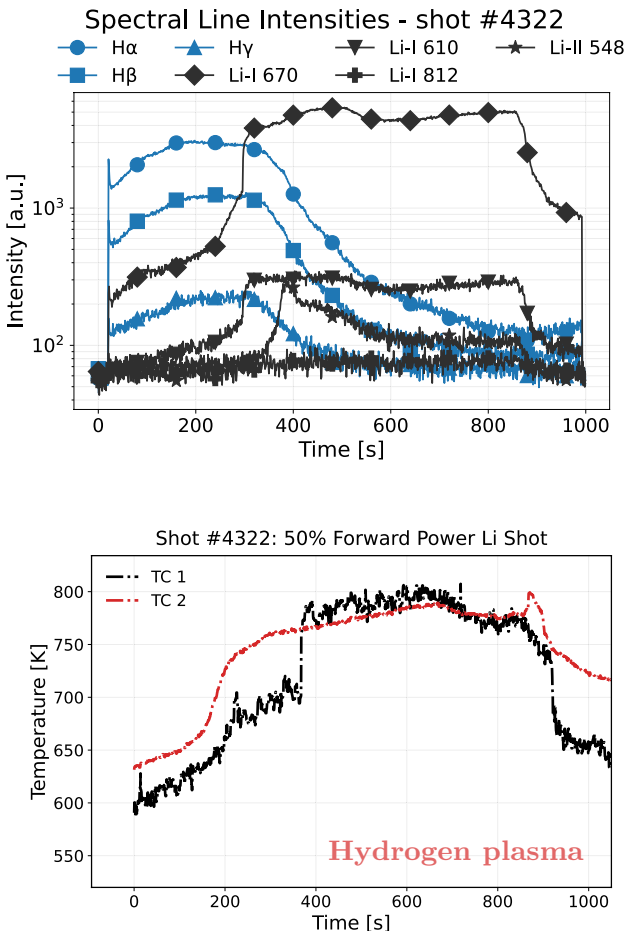

Fig. 14 Top: rise of lithium transitions at the expense of the hydrogen transitions during shot #4322. Bottom: corresponding surface temperature time evolution from both thermocouples (TC 1 and TC 2)

the nominal plasma fuel, producing a transition to a lithium-dominated plasma in every shot. Spectroscopic measurements consistently showed the growth of Li-I and Li-II lines at the expense of the hydrogen or helium lines, demonstrating that HIDRA's operational conditions allow only a narrow margin before lithium contamination becomes overwhelming. Even with the high retention fractions, the lithium impact on the plasma was severe.

These observations underscore the necessity of intercepting or containing lithium vapor before it can enter the core plasma. While trace lithium can be tolerated, and may even be beneficial to plasma operation, strong fuel dilution and impurity takeover, as observed on HIDRA, are undesirable. Given lithium's high evaporation rate, particularly at elevated surface temperatures, any successful experimental configuration must control the fraction of lithium entering the plasma relative to the total plasma volume and fueling rate. Approaches such as the lithium vapor box concept offer a promising path toward enabling controlled lithium experiments on HIDRA over a wider operational space.

Acknowledgements This work was supported by the U.S. Department of Energy under Grant No. DE-SC0017719, by the University of Illinois Urbana-Champaign Grainger College of Engineering, the Department of Nuclear, Plasma, and Radiological Engineering and the Office of the Vice Chancellor for Research and Innovation at the University of Illinois Urbana-Champaign. Work on this submission has received additional funding from Grants No. DE-SC0010529 and No. DE-FG02-07ER54917.

Author Contributions R.R. wrote the main manuscript text and prepared all the figures. R.R., A.S. and D.O'D. conducted the experiments. All authors contributed to the analysis of the experimental results. All authors reviewed the manuscript.

Data Availability All data supporting the findings of this study are available within the paper.

Declarations

Competing interests The authors declare no competing interests.

References

1. A. Loarte, B. Lipschultz, A. Kukushkin, G. Matthews, P. Stangeby, N. Asakura, G. Counsell, G. Federici, A. Kallenbach, K. Krieger, A. Mahdavi, V. Philipps, D. Reiter, J. Roth, J. Strachan, D. Whyte, R. Doerner, T. Eich, W. Fundamenski, A. Herrmann, M. Fenstermacher, P. Ghendrih, M. Groth, A. Kirschner, S. Konoshima, B. LaBombard, P. Lang, A. Leonard, P. Monier-Garbet, R. Neu, H. Pacher, B. Pegourie, R. Pitts, S. Takamura, J. Terry, E. Tsitrone, the ITPA Scrape-off Layer, D.P.T. Group, Chapter 4: power and particle control. Nucl. Fusion **47**(6), S203 (2007). https://doi.org/10.1088/0029-5515/47/6/S04
2. R. Nygren, F. Tabarés, Liquid surfaces for fusion plasma facing components-a critical review. Part I: Physics and PSI. Nucl. Mater. Energy **9**, 6–21 (2016). https://doi.org/10.1016/j.nme.2016.08.008
3. F.L. Tabarés, E. Oyarzabal, D. Tafalla, A. Martin-Rojo, D. Alegre, A. de Castro, First liquid lithium limiter biasing experiments in the TJ-II stellarator. J. Nucl. Mater. **463**, 1142–1146 (2015). https://doi.org/10.1016/j.jnucmat.2014.11.090
4. M. Baldwin, R. Doerner, S. Luckhardt, R. Conn, Deuterium retention in liquid lithium. Nucl. Fusion **42**(11), 1318 (2002). https://doi.org/10.1088/0029-5515/42/11/305
5. R. Majeski, R. Kaita, M. Boaz, P. Efthimion, T. Gray, B. Jones, D. Hoffman, H. Kugel, J. Menard, T. Munsat, A. Post-Zwicker, J. Spaleta, G. Taylor, J. Timberlake, R. Woolley, L. Zakharov, M. Finkenthal, D. Stutman, G. Antar, R. Doerner, S. Luckhardt,

R. Seraydarian, R. Maingi, M. Maiorano, S. Smith, D. Rodgers, V. Soukhanovskii, Testing of liquid lithium limiters in CDX-U. Fusion Eng. Des. **72**(1), 121–132 (2004). https://doi.org/10.1016/j.fusengdes.2004.07.002

6. A. Tuccillo, L. Amicucci, B. Angelini, M. Apicella, G. Apruzzese, E. Barbato, F. Belli, A. Bertocchi, A. Biancalani, A. Bierwage, W. Bin, L. Boncagni, A. Botrugno, G. Bracco, G. Breyannis, S. Briguglio, A. Bruschi, P. Buratti, G. Calabrò, A. Cardinali, C. Castaldo, S. Ceccuzzi, C. Centioli, R. Cesario, I. Chavdarovski, L. Chen, C. Cianfarani, S. Cirant, R. Coletti, F. Crisanti, O. D'Arcangelo, M. De Angeli, R. De Angelis, F. De Luca, L.D. Matteo, C.D. Troia, B. Esposito, G. Fogaccia, D. Frigione, V. Fusco, L. Gabellieri, A. Garavaglia, L. Garzotti, E. Giovannozzi, G. Granucci, G. Grossetti, G. Grosso, Z. Guimarães-Filho, F. Iannone, A. Jacchia, H. Kroegler, E. Lazzaro, M. Lontano, G. Maddaluno, M. Marinucci, D. Marocco, G. Mazzitelli, C. Mazzotta, A. Milovanov, F. Mirizzi, G. Monari, A. Moro, S. Nowak, F. Orsitto, D. Pacella, L. Panaccione, M. Panella, F. Pegoraro, V. Pericoli-Ridolfini, S. Podda, A. Pizzuto, G. Pucella, G. Ramogida, G. Ravera, M. Romanelli, A. Romano, G. Ramponi, C. Sozzi, G. Szepesi, E. Sternini, O. Tudisco, E. Vitale, G. Vlad, V. Zanza, M. Zerbini, F. Zonca, X. Wang, M. Aquilini, P. Cefali, E.D. Ferdinando, S.D. Giovenale, G. Giacomi, F. Gravanti, A. Grosso, V. Mellera, M. Mezzacappa, V. Muzzini, A. Pensa, P. Petrolini, V. Piergotti, B. Raspante, G. Rocchi, A. Sibio, B. Tilia, C. Torelli, R. Tulli, M. Vellucci, D. Zannetti, Overview of FTU results. Nucl. Fusion **51**(9), 094015 (2011). https://doi.org/10.1088/0029-5515/51/9/094015
7. J.C. Schmitt, R.E. Bell, D.P. Boyle, B. Esposti, R. Kaita, T. Kozub, B.P. LeBlanc, M. Lucia, R. Maingi, R. Majeski, E. Merino, S. Punjabi-Vinoth, G. Tchilingurian, A. Capece, B. Koel, J. Roszell, T.M. Biewer, T.K. Gray, S. Kubota, P. Beiersdorfer, K. Widmann, K. Tritz, High performance discharges in the Lithium Tokamak eXperiment with liquid lithium walls). Phys. Plasmas **22**(5), 056112 (2015). https://doi.org/10.1063/1.4921153
8. S. Mirnov, Plasma-wall interactions and plasma behaviour in fusion devices with liquid lithium plasma facing components. J. Nucl. Mater. **390–391**, 876–885 (2009). https://doi.org/10.1016/j.jnucmat.2009.01.228. (**Proceedings of the 18th International Conference on Plasma-Surface Interactions in Controlled Fusion Device**)
9. J. Hu, J. Ren, Z. Sun, G. Zuo, Q. Yang, J. Li, D. Mansfield, L. Zakharov, D. Ruzic, An overview of lithium experiments on HT-7 and EAST during 2012. Fusion Eng. Des. **89**(12), 2875–2885 (2014). https://doi.org/10.1016/j.fusengdes.2014.06.015
10. P. Lang, G. Conway, T. Eich, L. Fattorini, O. Gruber, S. Günter, L. Horton, S. Kalvin, A. Kallenbach, M. Kaufmann, G. Kocsis, A. Lorenz, M. Manso, M. Maraschek, V. Mertens, J. Neuhauser, I. Nunes, W. Schneider, W. Suttrop, H. Urano, the ASDEX Upgrade Team, ELM pace making and mitigation by pellet injection in ASDEX Upgrade. Nucl. Fusion **44**(5), 665 (2004). https://doi.org/10.1088/0029-5515/44/5/010
11. L. Baylor, N. Commaux, T. Jernigan, S. Combs, S. Meitner, N. Brooks, T. Evans, M. Fenstermacher, R. Isler, C. Lasnier, R. Moyer, T. Osborne, P. Parks, P. Snyder, E. Strait, E. Unterberg, A. Loarte, *High frequency ELM pacing by pellet injection on DIII-D and implications for ITER. 39th EPS Conference on Plasma Physics 2012, EPS 2012 and the 16th International Congress on Plasma Physics*, vol. 1 (2012), pp.81–84
12. T. Rognlien, M. Rensink, Interactions between liquid-wall vapor and edge plasmas. J. Nucl. Mater. **290–293**, 312–316 (2001). https://doi.org/10.1016/S0022-3115(00)00575-4
13. T. Morgan, A. Vertkov, K. Bystrov, I. Lyublinski, J. Genuit, G. Mazzitelli, Power handling of a liquid-metal based CPS structure under high steady-state heat and particle fluxes. Nucl. Mater. Energy **12**, 210–215 (2017). https://doi.org/10.1016/j.nme.2017.01.017
14. M. Ono, R. Majeski, M. Jaworski, Y. Hirooka, R. Kaita, T. Gray, R. Maingi, C. Skinner, M. Christenson, D. Ruzic, Liquid lithium loop system to solve challenging technology issues for fusion power plant. Nucl. Fusion **57**(11), 116056 (2017). https://doi.org/10.1088/1741-4326/aa7f41
15. M. Christenson, C. Moynihan, D. Ruzic, A distillation column for hydrogen isotope removal from liquid lithium. Fusion Eng. Des. **135**, 81–87 (2018). https://doi.org/10.1016/j.fusengdes.2018.07.009
16. T. Rognlien, M. Rensink, D. Stotler, Scrape-off layer plasma and neutral characteristics and their interactions with walls for FNSF. Fusion Eng. Des. **135**, 380–393 (2018). https://doi.org/10.1016/j.fusengdes.2017.07.024
17. E. Marenkov, A. Kukushkin, A. Pshenov, Modeling the vapor shielding of a liquid lithium divertor target using SOLPS 4.3 code. Nucl. Fusion **61**(3), 034001 (2021). https://doi.org/10.1088/1741-4326/abd642
18. A. Sestero, Protection of walls from hard disruptions in large tokamaks. Nucl. Fusion **17**(1), 115 (1977). https://doi.org/10.1088/0029-5515/17/1/011
19. G.G. van Eden, T.W. Morgan, D.U.B. Aussems, M.A. van den Berg, K. Bystrov, M.C.M. van de Sanden, Self-regulated plasma heat flux mitigation due to liquid Sn vapor shielding. Phys. Rev. Lett. **116**, 135002 (2016). https://doi.org/10.1103/PhysRevLett.116.135002
20. P. Rindt, T. Morgan, G. van Eden, M. Jaworski, N. Lopes Cardozo, Power handling and vapor shielding of pre-filled lithium divertor targets in Magnum-PSI. Nucl. Fusion **59**(5), 056003 (2019). https://doi.org/10.1088/1741-4326/ab0560
21. P. Rindt, S. Korving, T. Morgan, N. Lopes Cardozo, Performance of liquid-lithium-filled 3D-printed tungsten divertor targets under deuterium loading with ELM-like pulses in Magnum-PSI. Nucl. Fusion **61**(6), 066026 (2021). https://doi.org/10.1088/1741-4326/abf854
22. R. Rizkallah, Investigating the power dissipation mechanics in a lithium vapor cloud during vapor shielding regimes. Ph.D. thesis, University of Illinois Urbana-Champaign (2023). https://hdl.handle.net/2142/121314
23. G.G. van Eden, Vapour shielding of liquid metal walls in nuclear fusion devices. Ph.D. thesis, Technische Universiteit Eindhoven (2018). https://research.tue.nl/en/publications/vapour-shielding-of-liquid-metal-walls-in-nuclear-fusion-devices/. Proefschrift
24. P. Rindt, T. Morgan, M. Jaworski, N. Lopes Cardozo, Power handling limit of liquid lithium divertor targets. Nucl. Fusion **58**(10), 104002 (2018). https://doi.org/10.1088/1741-4326/aad290
25. P. Rindt, N. Lopes Cardozo, J. van Dommelen, R. Kaita, M. Jaworski, Conceptual design of a pre-loaded liquid lithium divertor target for NSTX-U. Fusion Eng. Des. **112**, 204–212 (2016). https://doi.org/10.1016/j.fusengdes.2016.08.020
26. S.K. Erents, G.M. McCracken, P. Goldsmith, Trapping of keV deuterons in lithium. J. Phys. D Appl. Phys. **4**(5), 672 (1971). https://doi.org/10.1088/0022-3727/4/5/305
27. A. Martin-Rojo, E. Oyarzabal, T. Morgan, F. Tabarés, Exposure of liquid lithium confined in a capillary structure to high plasma fluxes in PILOT-PSI-influence of temperature on D retention. Fusion Eng. Des. **117**, 222–225 (2017). https://doi.org/10.1016/j.fusengdes.2016.08.008
28. R. Rizkallah, D. Andruczyk, A. Shone, D. Johnson, Z. Jeckell, S. Marcinko, Z. Song, D. Curreli, F. Bedoya, A. Kapat, J.P. Allain, M. Christenson, M. Szott, S. Stemmley, H. Sandefur, D.N. Ruzic, R. Maingi, J. Hu, G. Zuo, J. Schmitt, Latest results from the Hybrid Illinois Device for Research and Applications (HIDRA). IEEE Trans. Plasma Sci. **46**(7), 2685–2690 (2018). https://doi.org/10.1109/TPS.2018.2838571

29. A. Shone, Z. Koyn, R. Rizkallah, D. O'Dea, A. Kapat, G. Golba, J. Hoffman, D. Kurukulasuriya, Q. Tang, A. de Castro, J.P. Allain, D. Andruczyk, An overview of the Hybrid Illinois Device for Research and Applications Material Analysis Test-stand (HIDRA-MAT). J. Fusion Energy **39**(6, SI), 448–454 (2020). https://doi.org/10.1007/s10894-020-00260-7
30. R. Rizkallah, S. Marcinko, D. Curreli, M. Parsons, N. Bartlett, R. Gluck, A. Shone, D. Andruczyk, Mapping of the HIDRA stellarator magnetic flux surfaces. Phys. Plasmas (2019). https://doi.org/10.1063/1.5100744
31. S. Marcinko, D. Curreli, Numerical characterization of the edge transport conditions and limiter fluxes of the HIDRA stellarator. Phys. Plasmas **25**(2), 022507 (2018). https://doi.org/10.1063/1.5018215
32. Y. Feng, F. Sardei, J. Kisslinger, 3D fluid modelling of the edge plasma by means of a Monte Carlo technique. J. Nucl. Mater. **266–269**, 812–818 (1999). https://doi.org/10.1016/S0022-3115(98)00844-7
33. Y. Feng, H. Frerichs, M. Kobayashi, A. Bader, F. Effenberg, D. Harting, H. Hoelbe, J. Huang, G. Kawamura, J.D. Lore, T. Lunt, D. Reiter, O. Schmitz, D. Sharma, Recent Improvements in the EMC3-Eirene Code. Contrib. Plasma Phys. **54**(4–6), 426–431 (2014). https://doi.org/10.1002/ctpp.201410092
34. K. Horvath, J. Lingertat, M. Laux, F. Wagner, Langmuir probe measurements in the WEGA Stellarator. Contrib. Plasma Phys. **44**(7–8), 650–655 (2004). https://doi.org/10.1002/ctpp.200410096
35. K. Horvath, J. Lingertat, M. Otte, F. Wagner, Investigations of the electron temperature profiles at the WEGA Stellarator. Plasma Phys. Control. Fusion **48**(2), 315 (2006). https://doi.org/10.1088/0741-3335/48/2/009
36. P.C. Stangeby, A problem in the interpretation of tokamak Langmuir probes when a fast electron component is present. Plasma Phys. Control. Fusion **37**(9), 1031 (1995). https://doi.org/10.1088/0741-3335/37/9/008
37. R. Mattas, J. Allain, R. Bastasz, J. Brooks, T. Evans, A. Hassanein, S. Luckhardt, K. McCarthy, P. Mioduszewski, R. Maingi, E. Mogahed, R. Moir, S. Molokov, N. Morely, R. Nygren, T. Rognlien, C. Reed, D. Ruzic, I. Sviatoslavsky, D. Sze, M. Tillack, M. Ulrickson, P. Wade, R. Wooley, C. Wong, ALPS–advanced limiter-divertor plasma-facing systems. Fusion Eng. Des. **49–50**, 127–134 (2000). https://doi.org/10.1016/S0920-3796(00)00385-9
38. A. Khodak, M.A. Jaworski, Parametric study of a divertor cooling system for a liquid-metal plasma-facing component. IEEE Trans. Plasma Sci. **42**(8), 2161–2165 (2014). https://doi.org/10.1109/TPS.2014.2330292
39. A. Khodak, R. Maingi, Modeling of liquid lithium flow in porous plasma facing material. Nucl. Mater. Energy **26**, 100935 (2021). https://doi.org/10.1016/j.nme.2021.100935
40. H.W. Davison, *Compilation of Thermophysical Properties of Liquid Lithium*, in *NASA Technical Note* (Lewis Research Center, Cleveland, Ohio, 1968). https://ntrs.nasa.gov/citations/19680018893
41. D. Jeppson, J. Ballif, W. Yuan, B. Chou, *Lithium literature review: lithium's properties and interactions* (Hanford Engineering Development Lab., Richland, Wash. (USA), 1978)
42. R. Ohse, I.U. of Pure, A. Physics, *Handbook of thermodynamic and transport properties of alkali metals*, vol. 30 (Blackwell Scientific Publications., 1985)
43. T. Abrams, M. Jaworski, R. Kaita, J. Nichols, G. De Temmerman, M. van den Berg, H. van der Meiden, T. Morgan, *Re-deposition of lithium and boron coatings under high-flux plasma bombardment at normal and grazing magnetic incidence*, in *2014 IEEE 41st International Conference on Plasma Sciences (ICOPS) held with 2014 IEEE International Conference on High-Power Particle Beams (BEAMS)* (2014), pp. 1–1. https://doi.org/10.1109/PLASMA.2014.7012276
44. D. Andruczyk, A. Shone, Z. Koyn, J. Allain, First lithium experiments in HIDRA and evidence of helium retention during quasi-steady-state stellarator plasma operations. Plasma Phys. Controlled Fusion (2022). https://doi.org/10.1088/1361-6587/ac7973
45. A. Shone, R. Rizkallah, D. O'Dea, K. B., D. Andruczyk, In-operando lithium evaporation inducing helium retention in long-pulse HIDRA helium plasmas. J. Fusion Energy **42**, 43 (2023). https://doi.org/10.1007/s10894-023-00383-7
46. R. Goldston, A. Hakim, G. Hammett, M. Jaworski, J. Schwartz, Recent advances towards a lithium vapor box divertor. Nucl. Mater. Energy **12**, 1118–1121 (2017). https://doi.org/10.1016/j.nme.2017.03.020. (**Proceedings of the 22nd International Conference on Plasma Surface Interactions 2016, 22nd PSI**)
47. E. Emdee, R. Goldston, J. Schwartz, M. Rensink, T. Rognlien, A simplified lithium vapor box divertor. Nucl. Fusion **59**(8), 086043 (2019). https://doi.org/10.1088/1741-4326/ab2825